

Improvement of Rain/No-Rain Classification Methods for Microwave Radiometer Observations over the Ocean Using a 37 GHz Emission Signature

Satoshi KIDA, Shoichi SHIGE

Department of Aerospace Engineering, Osaka Prefecture University, Sakai, Japan

Takuji KUBOTA

Earth Observation Research Center, Japan Aerospace Exploration Agency, Tsukuba, Japan

Kazumasa AONASHI

Meteorological Research Institute, Tsukuba, Japan

and

Ken'ichi OKAMOTO

Faculty of Environmental and Information Studies, Tottori University of Environmental Studies, Tottori, Japan

(Manuscript received 30 June 2008, in final form 5 November 2008)

Abstract

The rain/no-rain classification (RNC) for the Tropical Rainfall Measuring Mission (TRMM) Imager (TMI) fails in detecting shallow rain observed by the TRMM Precipitation Radar (PR). In this study, the RNC method is revised to use the 37-GHz emission more efficiently to identify shallow rain and is applied to the TMI observation. The results are then evaluated against the RNC made by the PR observation, considered as the “truth.” The revised RNC method (GSMAp2) is compared with the original RNC method (GSMAp1) and the Goddard profiling algorithm (GPROF).

GSMAp2 performs well for shallow rain behind cold fronts in the extratropics, where GSMAp1 and GPROF fail, using the 37-GHz emission signature. Through a whole year, a global comparison shows that GSMAp2 performs better than GSMAp1 and GPROF over mid-latitudes. However, GSMAp2 fails in detecting shallow isolated rain over sub-tropical oceans owing to a globally constant value for the vertically integrated cloud liquid water path (LWP) assumed in the forward calculation. Therefore, we parameterize the LWP as a function of storm height from the PR observation over the region where shallow isolated rain is predominant. GSMAp3, in which the parameterization of the LWP is applied to GSMAp2, improves detection of shallow isolated rain over sub-tropical oceans.

1. Introduction

Satellite-borne microwave radiometers provide observations of global precipitation. Rain estimation is important for the study of the global water cycle and water resources. Brightness temperatures (TBs) measured by these radiometers depend on the absorption

and scattering properties of the atmosphere and the underlying surface, which vary with frequency and polarization. There are generally two methods for estimating precipitation: one uses an emission signature from raindrops over the spectrum of lower frequencies (emission-based algorithm) and the other uses a scattering signature from ice crystals over the spectrum of higher frequencies (scattering-based algorithm).

A number of different microwave precipitation retrieval algorithms have been developed over the years.

Corresponding author: Satoshi Kida, Department of Aerospace Engineering, Osaka Prefecture University, 1-1 Gakuen-cho, Sakai, 599-8531, Japan
E-mail: kida@aero.osakafu-u.ac.jp
©2009, Meteorological Society of Japan

The methods of estimating precipitation from satellite-borne microwave radiometers are divided into two types. First, the empirical relationship between the TBs and the rainfall rate from ground radar datasets or rain gauges is used to estimate the rainfall rate. Although this method uses channels that have a high correlation with the rainfall rate, physical relationships between the rainfall rate and TBs are uncertain and this method is difficult to apply to global regions because the relationship may reflect the characteristics of the local regions.

Second, the relationship between TBs and rainfall rate established by the physical principles of radiative transfer is used to quantify the rainfall rate. This method clarifies the physical relationship between the rainfall rate and TBs and can be applied to various regions as long as the profiles of the various hydrometeors are appropriately represented. Generally, this method comprises two parts: a forward calculation and retrievals. In the forward calculation, lookup tables (LUTs) or databases showing the relationship between rainfall rates and TBs are produced using radiative transfer models (RTMs). A retrieval consists of a rain/no-rain classification (RNC) and an estimation of the rain rates over the delineated rainy area.

This study focuses on the RNC. For the RNC over land, only the scattering-based algorithm is used because the contrast between surface and atmosphere becoming smaller, owing to high emissivity over land, makes it difficult to apply the emission-based algorithm. In contrast, for the RNC over the ocean, either the emission-based algorithm or the scattering-based algorithm can be used because of the low emissivity over the ocean. Therefore, the RNC over the ocean has higher accuracy than the RNC over land. However, the RNC over the ocean has uncertainty for shallow rain. Petty (1997) indicated that Special Sensor Microwave/Imager (SSM/I) rainfall algorithms have difficulty detecting small rain areas. This difficulty is due to the scale of the rain being smaller than the 30 to 60 km resolution of the SSM/I channels used in most emission-based algorithms. Petty (1997) suggested that the only hope of directly sensing such precipitation is to use the 85-GHz channel for an emission-based algorithm, which is often used for a scattering-based algorithm, because it has the highest resolution (15 km) among the SSM/I channels.

The Tropical Rainfall Measuring Mission (TRMM) carries two microwave sensors on the same platform for quantitative rainfall measurement: the precipitation radar (PR) and the TRMM microwave imager (TMI)

(Kummerow et al. 1998). The PR is a nadir-looking Precipitation Radar that measures back-scatter from precipitation particles (Kozu et al. 2001; Okamoto 2003; Okamoto and Shige 2008). The PR observes the three-dimensional structure of precipitation at a fine resolution (~4 km) with a 215 km-wide swath. The TMI is a nine-channel passive microwave radiometer based on the SSM/I, with a 720 km-wide swath. One key difference is the addition of a pair of 10-GHz channels with horizontal and vertical polarizations, denoted as 10H and 10V. Another key difference is that the spatial resolution of TMI is improved over that of SSM/I. Using simultaneous observations by the PR and TMI allows us to improve the retrieval of rain from measured TBs.

We develop a microwave precipitation retrieval algorithm (Global Satellite Mapping of Precipitation, GSMaP) compatible with the PR algorithm (Aonashi et al. 1996; Aonashi et al. 2009; Kubota et al. 2007), based on the deterministic rain-retrieval algorithm of Aonashi and Liu (1998). The GSMaP algorithm is used by the Earth Observation Research Center, Japan Aerospace Exploration Agency (JAXA/EORC) to offer hourly global rainfall maps in near real time., The GSMaP algorithm is used by Shige et al. (2008) for scientific study. The GSMaP products are available on the Internet at <http://www.radar.aero.osakafu-u.ac.jp/~gsmmap/>. The RNC method over land used in GSMaP was developed using statistical information for TMI TBs under no-rain conditions from PR observations (Seto et al. 2005). In the RNC method over the ocean, rainfall is classified mostly by the 10- and 19-GHz emission signatures and the 85-GHz scattering signature.

Over the ocean, the RNC for the TMI fails in detecting shallow rain observed by PR because shallow rain has a scale smaller than the resolution of the channels used in the emission-based algorithm and has little ice aloft. Here, we define shallow rain as having a small scale (~20 km) and a precipitation top height lower than the freezing level height (FLH). We define deep rain as having a larger scale and a precipitation top height higher than the FLH.

It is very difficult to use the 85-GHz emission-based algorithm to detect shallow rain because clouds are optically thick at 85-GHz. The resolution of the microwave radiometer has advanced with improvements in the technology and resolution of the 37-GHz channel (~16 km) of the TMI, such that the resolution is now comparable with that of the 85-GHz channel (~15 km) of the SSM/I. Therefore, the shallow rain

indicated by Petty (1997) is expected to be directly detected using the 37-GHz channels of the TMI for the emission-based algorithm in the RNC method.

This study aims at improving the RNC over the ocean for GSMaP using the 37-GHz channel of the TMI in an emission-based algorithm. The revised RNC method is evaluated by comparing it with the RNC from the PR. The datasets used in this study are described in Section 2. We review the RNC method of the Goddard profiling algorithm (GPROF) and the original RNC method of GSMaP in Section 3. In Section 4, we revise the RNC method of GSMaP to use the 37-GHz emission signature more efficiently. We also investigate the performance of the revised RNC method using two case studies and global comparisons. In Section 5, we improve the forward model, which the RNC method depends on, over subtropical oceans. Summaries are given in Section 6.

2. Data

In this study, we focus on GSMaP for the TMI (GSMaP_TMI), because GSMaP_TMI results can be compared with the PR observations. In the forward model, LUTs are produced using the four-stream RTM of Liu (1998). The RTM is inputted with atmospheric variables (freezing height, temperature, relative humidity, surface wind, and surface temperature) provided by the Japan Meteorological Agency Global Analysis (GANAL). In the cloud layer under the FLH, constant values for the vertically integrated cloud liquid water content (LWP) (0.5 kg m^{-2}) and relative humidity (100%) are assumed (Aonashi and Liu 1998). LUTs are calculated for each 5×5 -degree latitude-longitude box. The RTM is also inputted with a set of hydrometeor profiles given by PR observation. The PR-observed hydrometeor profiles are classified into ten precipitation types. The precipitation types are determined using the stratiform pixel ratio, stratiform rain ratio, precipitation area, precipitation-top height, rain intensity, and diurnal cycle from PR 2A25 along with the TRMM Lightning Imaging Sensor flash rates (Takayabu and Katayama 2004; Takayabu 2006). There are six land precipitation types (severe thunderstorm, afternoon shower, shallow rain, extratropical frontal system, organized system, and high land rain) and four ocean precipitation types (shallow rain, extratropical frontal system, transition zone, and organized system).

For comparison with GSMaP_TMI we used the current (version 6) level-2 standard products of the PR and TMI published by the National Aeronautics and

Space Administration and the Japan Aerospace Exploration Agency. The level-2 standard product 2A12 (GPROF) (Olson et al. 2006) was used for the rain estimation of the TMI. The basis of GPROF is a Bayesian framework in which retrieved precipitation is constructed from cloud-resolving model-generated profiles that are radiatively consistent with observation. The level-2 standard product 2A25 (Iguchi 2007; Iguchi et al. 2009) was used for the rain estimation of the PR. We used 2A25 as the truth for the RNC in this study because the resolution of the PR is higher than that of the TMI. In order to more directly compare the relatively high-resolution PR observations with the estimation from the TMI, we matched the resolution of the PR with that of the 85-GHz TMI data. A weighted average of the PR observations in the neighborhood of a given TMI footprint is performed. The PR average rainfall rate is defined by

$$R_{ave} = \frac{\sum_j g_j R_j}{\sum_j g_j}, \quad (1)$$

where R_j is the near-surface rain from PR2A25, and

$$g_j = \exp\left[-\ln(2) \left\{ \left(\frac{x}{\sigma_x} \right)^2 + \left(\frac{y}{\sigma_y} \right)^2 \right\} \right], \quad (2)$$

is a Gaussian weighting factor. Here, because the TMI footprint takes the form of an ellipse, if the short axis direction and the long axis direction are defined as the x -direction and y -direction, then x and y are the distances in kilometers between the PR footprint (indexed by j) and the specified TMI footprint. The long axis σ_x and the short axis σ_y , which are the half-footprint dimensions of the TMI 85-GHz channels, are 2.3 km and 3.6 km. The average value of the PR rainfall rate is used throughout the paper. The comparison with these products is processed in the PR swath, although both GSMaP and GPROF were applied to the TMI swath.

3. RNC method

In this section, the RNC methods for GPROF and the original GSMaP are reviewed briefly. The original RNC method of GSMaP is referred to as GSMaP1. Because the RNC of GPROF is determined after each

pixel is processed using screening and the full Bayesian code, we consider the RNC method of GPROF to consist of these processes.

3.1 RNC method of GPROF over the ocean

In GPROF, screening is performed in order to identify regions that are non-raining. All pixels that pass this screening are identified as “possibly rain” and are then processed using the full Bayesian algorithm to quantify the rain rate, which could be zero or non-zero.

The screening of GPROF over the ocean consists of two processes: checking the LWP and screening out clear ocean pixels and ice surface pixels (Fig. 1).

In the first process, the LWP (kg m^{-2}) is estimated using the observed 22V and 37V TBs (denoted as TB22V and TB37V), based on the work by Karstens et al. (1994):

$$LWP = 0.399635 \log(285 - TB22V) - 1.40692 \log(285 - TB37V) + 4.299. \quad (3)$$

The maximum LWP (LWP_{max}) (kg m^{-2}) based on

the FLH (m) is defined as

$$LWP_{\text{max}} = 0.25 \times \frac{FLH}{4000}, \quad (4)$$

where FLH is derived from the work by Wilheit et al. (1991), the constant values of 0.25 and 4000 represent the liquid water content (kg m^{-3}) and a typical freezing level height (m). If the LWP is less than LWP_{max} for a target pixel, then that pixel is identified as a no-rain pixel.

The second process is based on the Goddard Scattering (GSCAT) algorithm (Adler et al. 1994). This process consists of three checks. The first check is given by

$$TB85H > 262.0, \text{ and } TB22V < 269.1. \quad (5)$$

If this condition is fulfilled for a target pixel, that pixel is identified as possibly rain. This check was originally intended to detect ambiguity between the signals from an ice surface and possible rain, but it is used to detect rain in GPROF version 6.

The second check is to distinguish ice surfaces from rain and is given by

$$TB22V < 192.0. \quad (6)$$

If this condition is fulfilled for a target pixel, that pixel is identified as an ice surface.

The third check is to identify clear ocean and is given by

$$TB85H - TB37H > 0.5, \text{ and } TB37H \leq 186.7. \quad (7)$$

If this condition is fulfilled for a target pixel, that pixel is identified as clear ocean.

If the target pixel is not identified as an ice surface or clear ocean by these checks, then it is identified as possible rain.

After the screening, possible rain pixels are processed using the full Bayesian algorithm to quantify the rain rate, which could be zero or non-zero.

3.2 Original RNC method of GSMaP over the ocean (GSMaPI)

GSMaPI over the ocean consists of two stages (Fig.

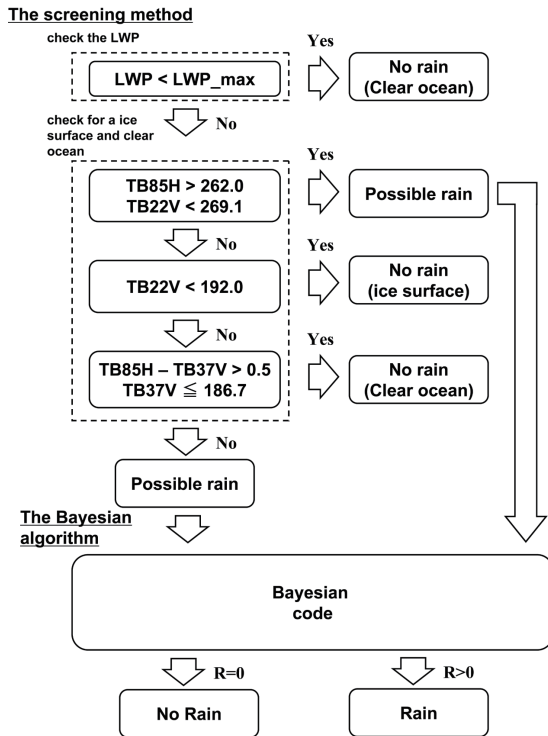


Fig. 1. Flowchart for the RNC method of GPROF over the ocean.

2a). In the first stage, we divide the pixels into deep-rain pixels and shallow-rain pixels. The deep-rain pixels are determined by the 85-GHz scattering signature and the shallow-rain pixels are determined by the 37-GHz emission signature.

To detect a deep-rain pixel, a first guess of the precipitation (rain85) for all pixels within the 10-GHz effective field of view (EFOV) (a large ellipse, as seen in Fig. 2b) with a central target pixel (the black ellipse in Fig. 2b) is computed from the observed polarization-corrected temperature (PCT) (Spencer et al. 1989) at 85-GHz (PCT85), using the LUTs. If rain85 is greater than 1 mm h⁻¹ for any pixels within the 10-GHz EFOV of the central target pixel, the target pixel is identified as a deep-rain pixel. (Hereafter, this identification procedure is referred to as FOV10on.) The aim of using FOV10on is to search for stratiform rain occurring near convective rain.

If the target pixel is not a deep-rain pixel, the 37-GHz emission signature is checked to determine whether the pixel is a shallow-rain or no-rain pixel. To detect a shallow-rain pixel, we use the normalized polarization difference (Petty 1994) at 37-GHz (P37) given by

$$P37 = \frac{TB37V - TB37H}{TB37Vo - TB37Ho}, \tag{8}$$

where TB37Vo and TB37Ho are TB37V and TB37H in a rain-free region. In computing P37, the TB37V and TB37H at 0 mm h⁻¹ in the LUTs, simulated using GANAL and cloud water, are used as TB37Vo and TB37Ho. The condition for the determination of a shallow-rain pixel is

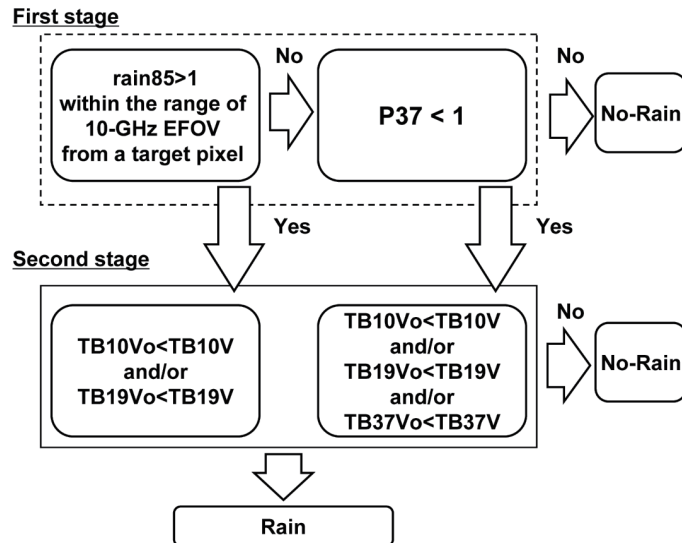
$$P37 < 1, \tag{9}$$

because P37 decreases from 1 as the rainfall rate increases.

According to the results of the first stage of the RNC method, emission signatures from raindrops are checked in the second stage. For deep-rain pixels, TB10V and TB19V are used with the conditions given by

$$TB10V > TB10Vo, \text{ or } TB19V > TB19Vo. \tag{10}$$

(a) GSMaP1



(b) FOV10on

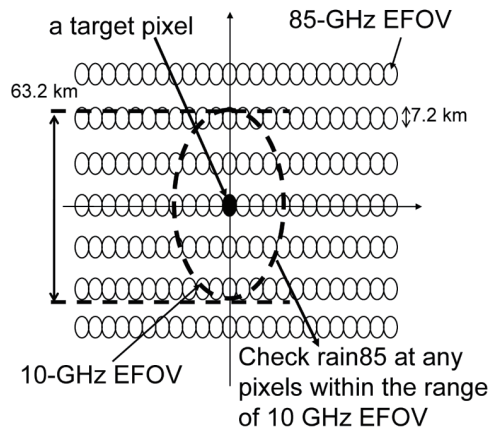


Fig. 2. (a) Flowchart for GSMaP1 and (b) schematic diagram of FOV10on. The small ellipse (solid curve) indicates the 85-GHz EFOV. The large ellipse (dashed curve) indicates the 10-GHz EFOV. The black pixel is the target pixel.

For shallow-rain pixels, TB37V is additionally used because the scattering from ice particles is not pre-dominant in shallow rain. The condition is given by

$$TB10V > TB10Vo, \text{ or } TB19V > TB19Vo, \\ \text{ or } TB37V > TB37Vo. \quad (11)$$

4. Improvement of the RNC method

In this section, we revise the RNC method of GSMaP for retrievals (Fig. 3a). We use the 37-GHz emission signatures more efficiently in the revised RNC method, referred to as GSMaP2. We also investigate the performance of GSMaP2 using two case studies and a global comparison.

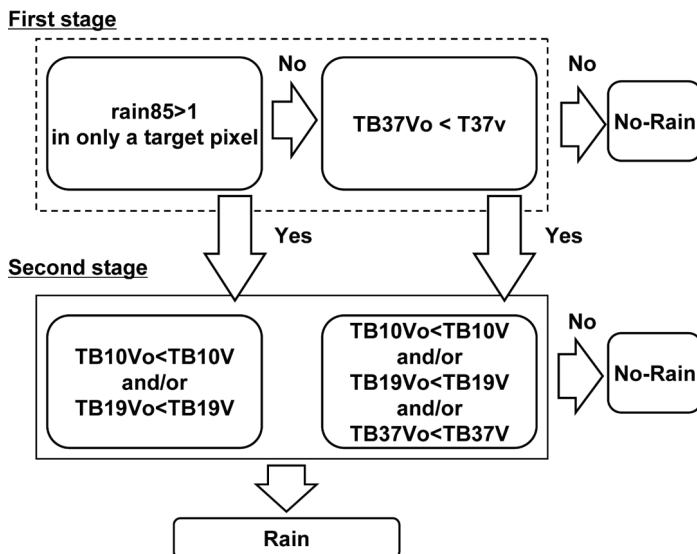
4.1 Revised RNC method of GSMaP (GSMaP2)

This study modifies two conditions (FOV10on and P37<1) in the first stage of GSMaP1 in order to use 37-GHz emission signatures more efficiently. When there are pixels whose rain85 is greater than 1mm hr⁻¹ within the 10-GHz EFOV, the central target pixel is classified as a deep-rain pixel in FOV10on of GSMaP1 even if it is actually a shallow-rain pixel (Fig. 4).

When a shallow-rain pixel is misclassified as a deep-rain pixel, the emission signatures of the shallow-rain pixel are checked using TB10V and TB19V, which have weaker signatures due to the lower resolution of these channels compared with the scale of the shallow rain. As a result, most shallow-rain pixels are misclassified as no-rain pixels. Therefore, rain85 is checked only for the target pixel (Fig. 3b). Rain85 is not checked for other pixels in the 10-GHz EFOV. (Hereafter, this procedure is referred to as FOV10off.)

TB37V is used instead of P37 to detect shallow-rain pixels. TB37H is more sensitive to wind speed than TB37V (Fig. 5). In a windy region, the difference between TB37V and TB37H (denoted as dTB37) is less, because TB37H, which is in P37, increases more than TB37V does as the wind speed increases. In the forward calculation, the difference between TB37Vo and TB37Ho (denoted as dTB37o) is computed using the averaged wind speed in the 5 × 5-degree latitude-longitude boxes from GANAL. If there is an extraordinary event (e.g., a typhoon), dTB37 will be less than dTB37o in a windy region with non-precipitation because the local wind speed is larger than the averaged wind speed from GANAL. As a result, P37 is less than 1, leading to a misclassification of the shallow rain in the windy region. Therefore,

(a) GSMaP2



(b) FOV10off

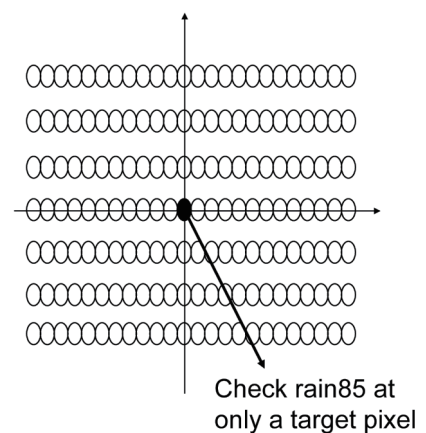


Fig. 3. (a) Flowchart for GSMaP2 and (b) schematic diagram of FOV10off.

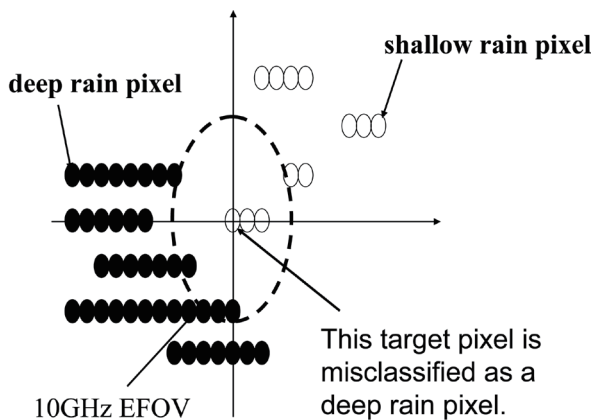


Fig. 4. Typical example of a shallow-rain pixel being misclassified as a deep-rain pixel. Gray ellipse indicates a deep-rain pixel; white ellipse indicates a shallow-rain pixel.

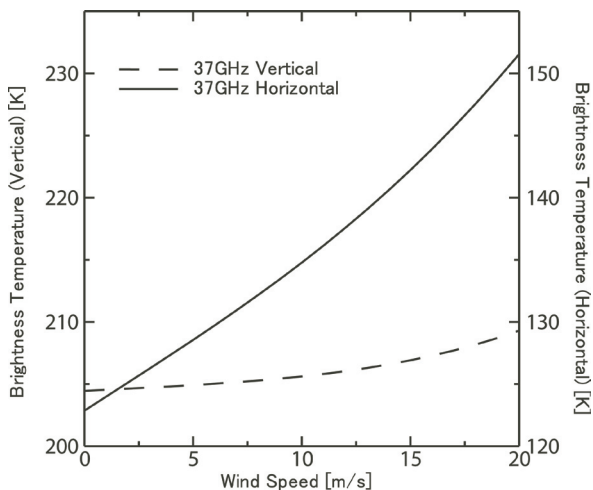


Fig. 5. TB37H (solid line, scale on the right vertical axis) and TB37V (dashed line, scale on the left vertical axis) as functions of wind speed.

only TB37V, which is less sensitive to variability of wind speed, is used for detecting shallow rain. The condition is given by

$$TB37V > TB37V_o. \tag{12}$$

4.2 Performance of GSMaP2

The performance of GSMaP2 is compared with that of GSMaP1 and GPROF. To evaluate the performance of the RNC, we introduce the equitable threat score (ETS) (Schaefer 1990; Wilks 2006) because we are focusing not on the estimation of rain but on the RNC. ETS is defined by

$$ETS = \frac{N_1 - N_{ref}}{N_1 - N_{ref} + N_2 + N_3},$$

$$N_{ref} = \frac{(N_1 + N_2)(N_1 + N_3)}{N_1 + N_2 + N_3 + N_4}, \tag{13}$$

where N_1 is the number of pixels where rain observed by PR exists and the RNC method classifies rain, N_2 is the number of pixels where rain exists and the RNC method classifies no-rain, N_3 is the number of pixels where rain does not exist and the RNC method classifies rain, and N_4 is the number of pixels where rain does not exist and the RNC method classifies no-rain. The ETS ranges from $-1/3$ to 1 with the best possible ETS being 1.

We investigated the performance of the RNC methods in two cases. In the first case, rain is scattered over the sea east of Japan (30°N – 36°N , 145°E – 160°E) (hereafter case 1). The other case is typhoon Olga over the western Pacific (17°N – 29°N , 125°E – 137°E) (hereafter case 2).

In case 1, the PR observed scattered rain behind cold fronts in the extratropics (Fig. 6a). Figure 7 presents a vertical cross-section along the A–A' line in Fig. 6a. The cloud tops observed by Visible Infrared Scanner (VIRS) aboard TRMM reach about 4 km in altitude, but the scattered rain top is very shallow (~3 km). The ETS values of GPROF, GSMaP1, and GSMaP2 are 0.116, 0.132, and 0.284 respectively. Although the results of the three RNC methods coincide with the PR results in the broad rain region around 34°N , 150°E , detection of the scattered rain is different among the three RNC methods. In GSMaP1, the rain pixels are not scattered but broad (Fig. 6c) because the pixels around the deep-rain pixel are misclassified as rain pixels by FOV10on. In contrast, scattered shallow rain is detected well by FOV10off in GSMaP2 (Fig. 6d) because FOV10off has a greater chance of detecting shallow rain using the emission signal at 37-GHz than FOV10on does. Some scattered rain is detected by GPROF, but there are fewer such rain pixels than in the PR results (Fig. 6b). Berg et al.

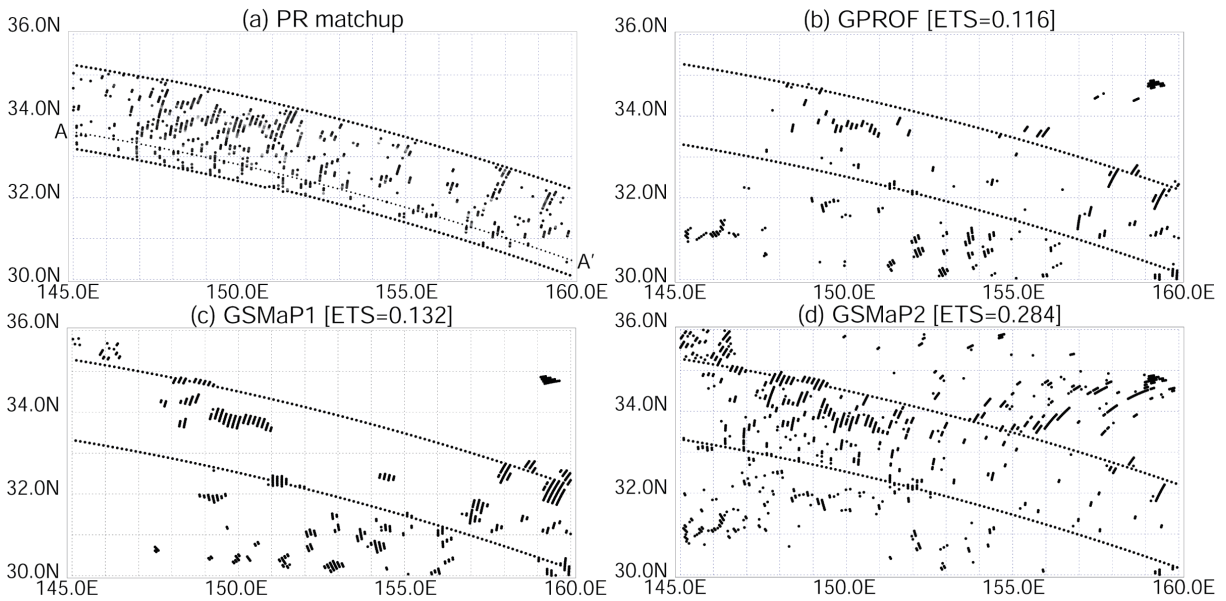


Fig. 6. Case 1 of scattered rain associated with a post-frontal convective system for 10 January 1999 (TRMM orbit number 6436) over the sea east of Japan (30°N–36°N, 145°E–160°E).

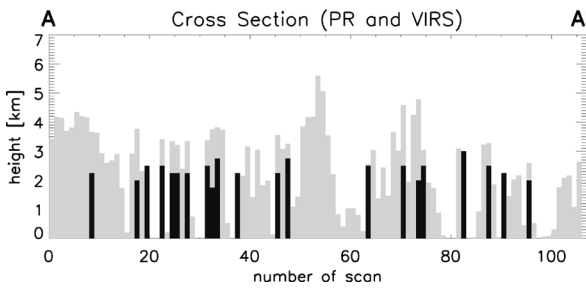


Fig. 7. Vertical cross-section along the A–A' line in Fig. 6a. Black bars indicate the rain height of the PR observation; gray bars indicate cloud heights estimated by the Visible Infrared Scanner (VIRS).

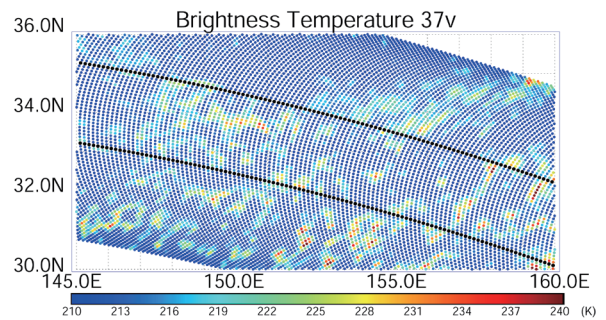


Fig. 8. Brightness temperature at 37 GHz, from the TMI observation for the case in Fig. 6.

(2005) suggested that GPROF consistently misses rainfall events behind cold fronts in the extratropics because these systems are spatially too small to be properly captured by the relatively large TMI footprint. However, the 37-GHz emission signature nearly corresponds to the rain pixels detected by PR, as seen in Fig. 8. In GPROF, the constant threshold of TB37H used in condition (7) is less than the observed TB37H for shallow rain, leading to the misclassification of the shallow rain. GPROF may be tuned for the tropics and

may not be applicable to systems over mid-latitude. In contrast, the regional threshold of TB37V of the RNC using GANAL is used in GSMaP2, and thus shallow rain can be detected by GSMaP2.

In case 2, the PR observed rain bands associated with typhoon Olga (Fig. 9a). The ETS of GPROF is 0.434 (Fig. 9b), the ETS of GSMaP1 is 0.303 (Fig. 9c), and the ETS of GSMaP2 is 0.505 (Fig. 9d). GSMaP2 and GPROF produce better results than GSMaP1. GSMaP1 tends to overestimate extended rainy regions

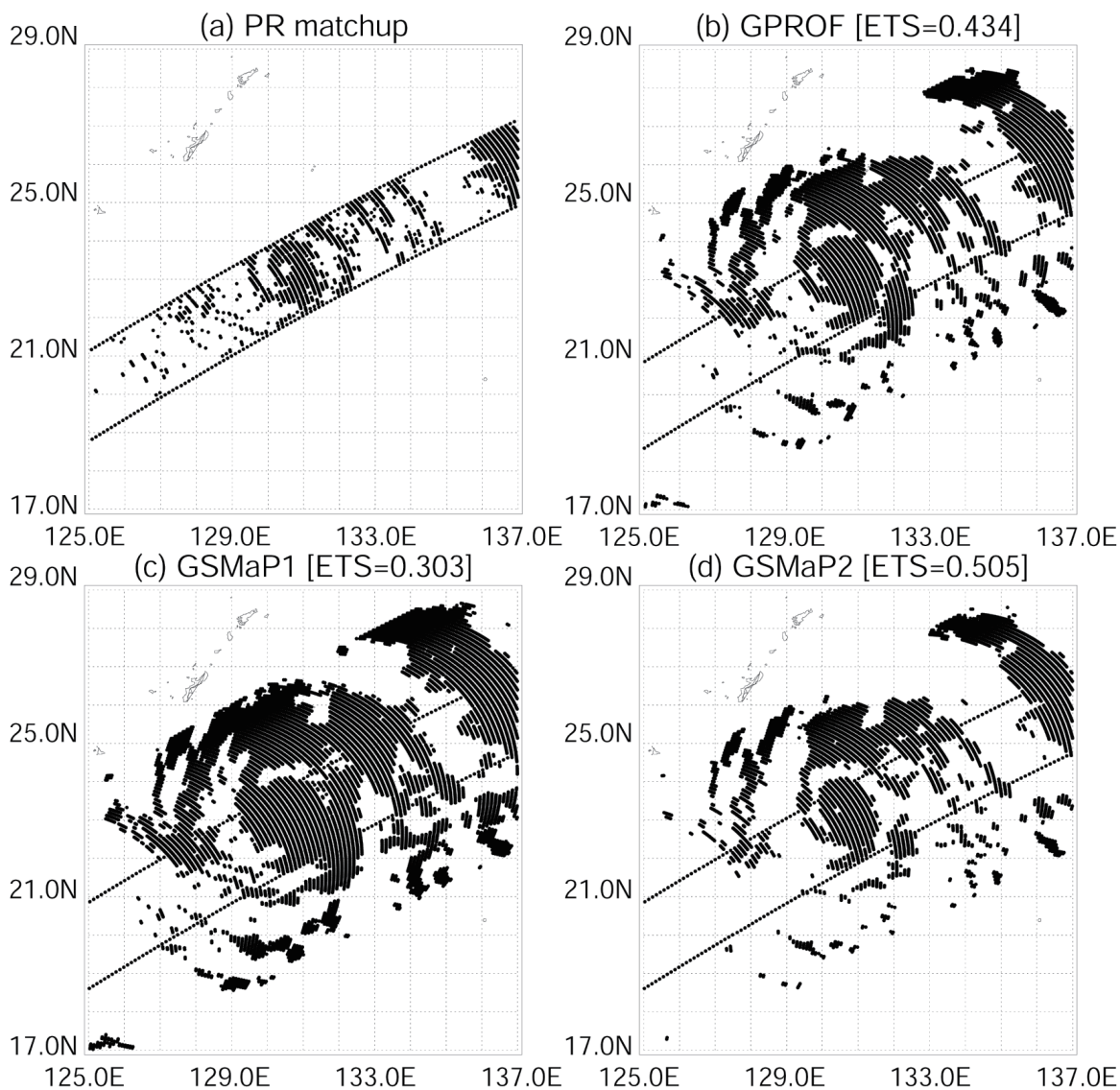


Fig. 9. Case 2 of typhoon Olga for 31 July 1999 (TRMM orbit number 9629) over the western Pacific (17°N–29°N, 125°E–137°E).

where GSMaP2 and GPROF classify no-rain. The overestimates of GSMaP1 are caused by P37. In a windy region such as one where there is a typhoon, $dTB37$ decreases because $TB37H$ increases with wind speed more than $TB37V$ does (Fig. 5). On the other hand, $dTB37o$ is computed from GANAL using the average wind speed in the 5×5 -degree latitude-longitude box. The averaged wind speed should be weaker than the local wind speed. Therefore, $dTB37$ is less than $dTB37o$ in a windy region. As a result, P37 is

less than 1 and the windy region is misclassified as a rainy region. The ETS of GSMaP2 is higher than that of GPROF because GPROF produces a larger rainy region than the PR. The screening in GPROF tends to classify regions that are larger than the PR region as “possibly raining.” Although the region identified as “possibly raining” consists of both raining and non-raining regions, in the Bayesian algorithm, these regions are identified as raining regions because the database that is used in the Bayesian algorithm rep-

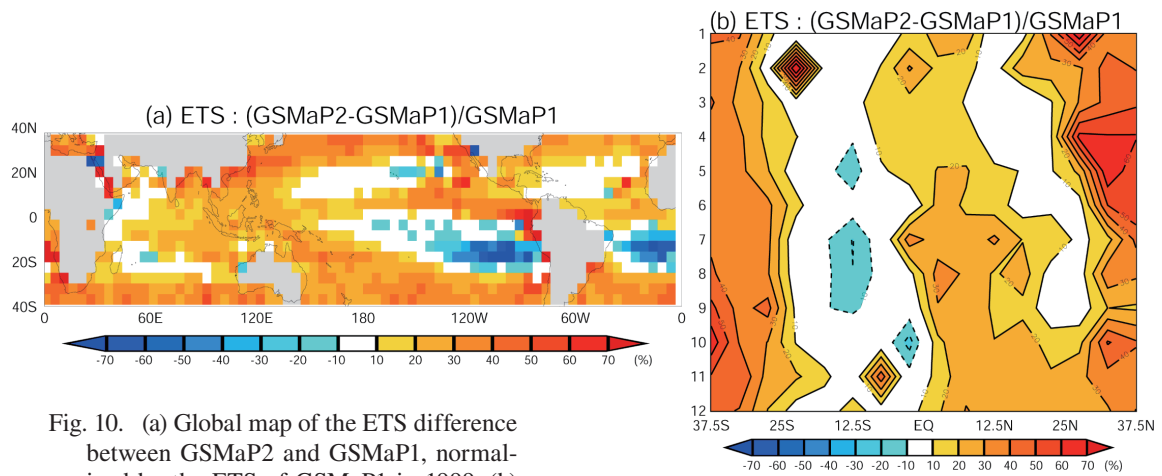


Fig. 10. (a) Global map of the ETS difference between GSMaP2 and GSMaP1, normalized by the ETS of GSMaP1 in 1999. (b) Hovmöller diagram of the monthly zonal average of the ETS difference between GSMaP2 and GSMaP1.

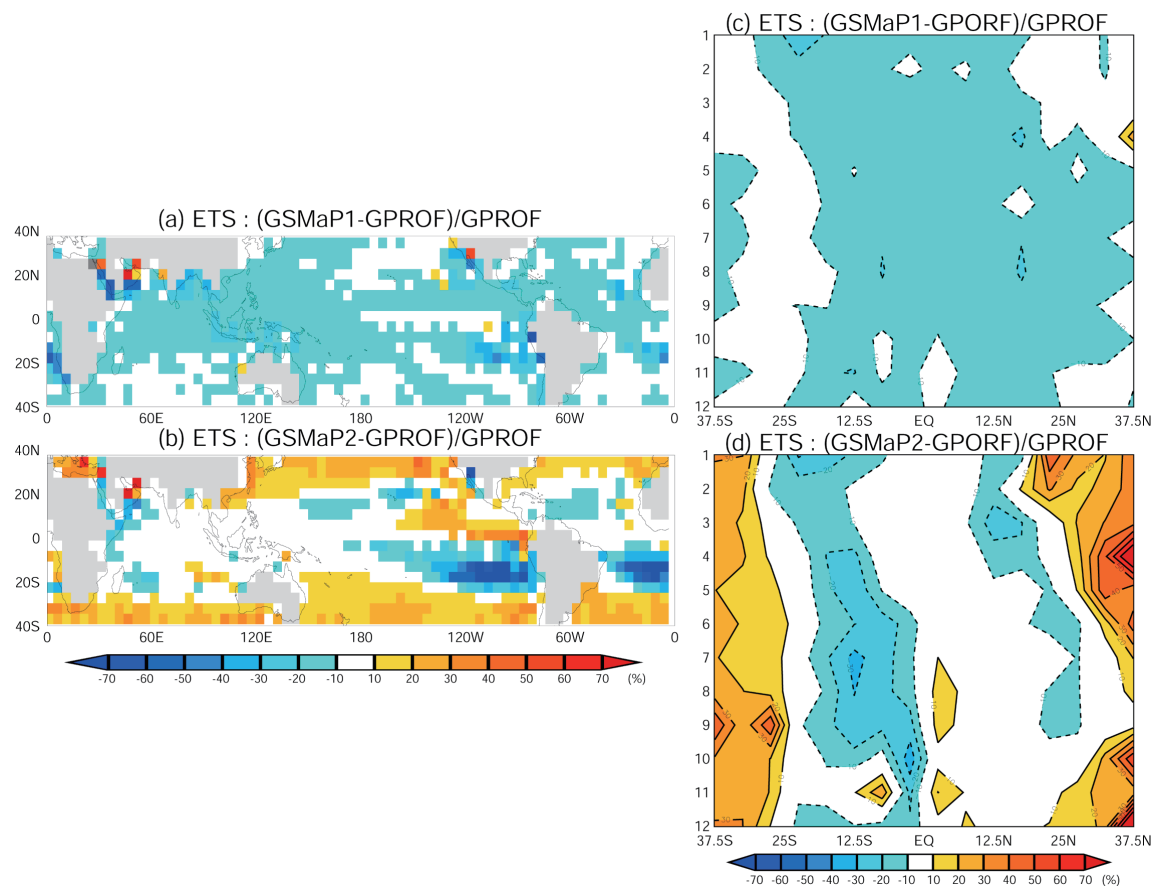


Fig. 11. ETS difference between GSMaP and GPROF, normalized by the ETS of GPROF in 1999. The ETS difference is between GPROF and (a) GSMaP1 and (b) GSMaP2. Hovmöller diagram of the monthly zonal average of the ETS difference between GSMaP and GPROF, normalized by the ETS of GPROF in 1999. The ETS difference is between GPROF and (c) GSMaP1 and (d) GSMaP2.

resents only a small fraction of the systems that might be observed by the TMI.

A global comparison of GPROF, GSMaP1, and GSMaP2 is performed using the ETS for 1999. Figure 10a illustrates the difference in the ETS values for GSMaP2 and GSMaP1, normalized by the ETS of GSMaP1. Over mid-latitudes, GSMaP2 performs better than GSMaP1 because GSMaP2 has improved the RNC for scattered shallow rain. Over the tropics, GSMaP2 also performs better than GSMaP1 because the overestimates of rainy regions in GSMaP1 are reduced in GSMaP2. In contrast, the ETS values of GSMaP2 decrease over sub-tropical oceans because of the failure to detect shallow rain. Figure 10b is a Hovmöller diagram of zonal average ETS values in 1999. The ETS values of GSMaP2 are higher than those of GSMaP1 over both mid-latitudes and tropics through the whole year. The highest ETS of GSMaP2

is found over mid-latitudes in winter. In contrast, the lowest ETS of GSMaP2 is found over sub-tropical oceans in winter. Figures 11a and 11b illustrate the difference in the ETS values for GSMaP and GPROF, normalized by the ETS of GPROF. While the ETS values of GSMaP1 are lower than those of GPROF in almost every region, the ETS values of GSMaP2 are higher than those of GPROF over mid-latitudes. Over mid-latitudes, there is a horizontal non-uniformity of environments because the winter mid-latitudes are affected by strong baroclinic waves and fronts. A regionally varying threshold value for the RNC using GANAL is computed in GSMaP2, while GPROF sets the constant threshold value globally. Therefore, GSMaP2 performs well for mid-latitudes. Figures 11c and 11d are Hovmöller diagrams of zonal average ETS values for GSMaP1 and GSMaP2. The ETS values of GSMaP1 are lower than those of GPROF through the

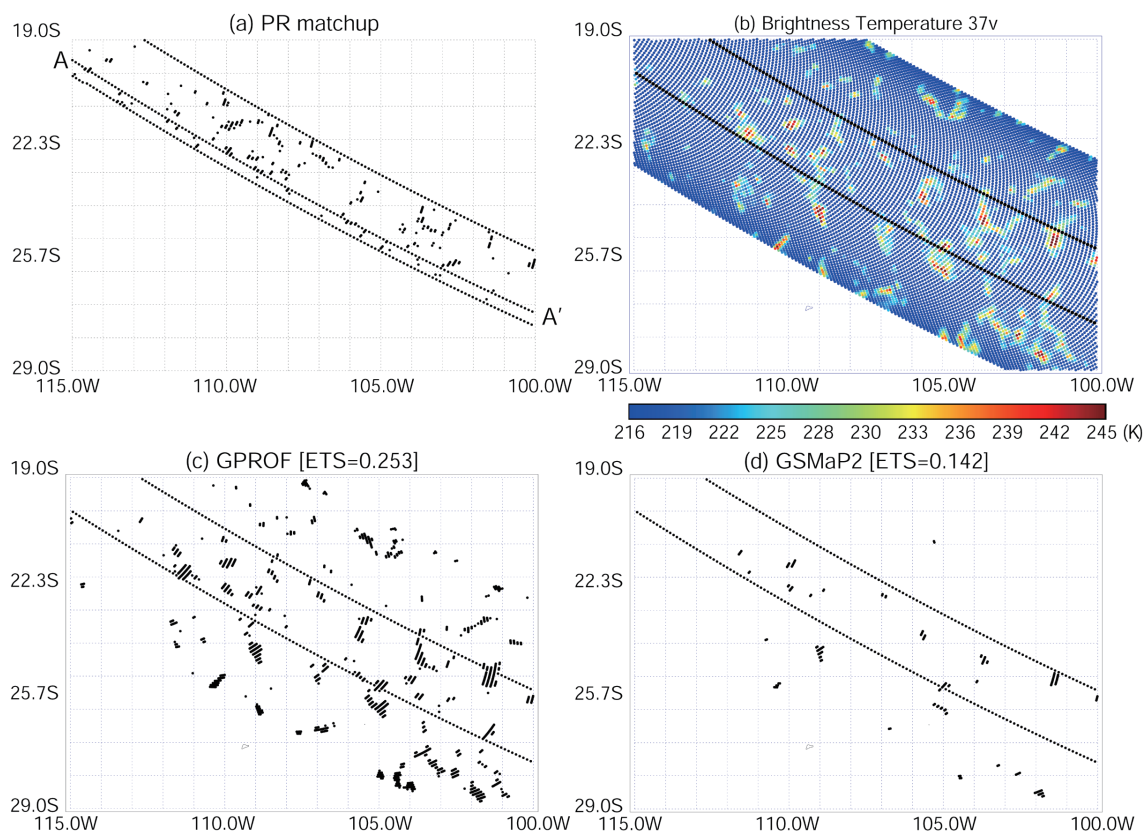


Fig. 12. Shallow rain over sub-tropical ocean (19°S–9°S, 100°W–115°W) for 30 January 1999 (TRMM orbit number 6760). (a) Rain from the PR observation. (b) TB37V from the TMI observation. (c) GPROF. (d) GSMaP2.

whole year. However, the ETS values of GSMaP2 are higher than those of GPROF over the mid-latitudes. Over the tropics, GSMaP2 performs as well as GPROF does. Over sub-tropical oceans, the ETS values of GSMaP2 are lower than those of GPROF. This is caused by the failure to detect shallow rain over sub-tropical oceans and will be addressed in the following section.

5. Improvement of the LWP in the forward model

5.1 Parameterization of the LWP over sub-tropical ocean (GSMaP3)

Figure 12 illustrates the case of shallow rain over sub-tropical ocean. It is found that the emission signatures at 37V (Fig. 12b) almost corresponds to the rain pixels determined by the PR (Fig. 12a). The shallow rain is detected in GPROF (Fig. 12c). However, in GSMaP2, most of the shallow-rain areas are misclassified as no-rain areas (Fig. 12d). Figure 13 is a scatter plot between the rainfall rate as estimated by PR and TB37V as observed by TMI. The relationship between TB37V and the surface rainfall in the LUT at the grid point 107.5°W, 22.5°S used in this region is

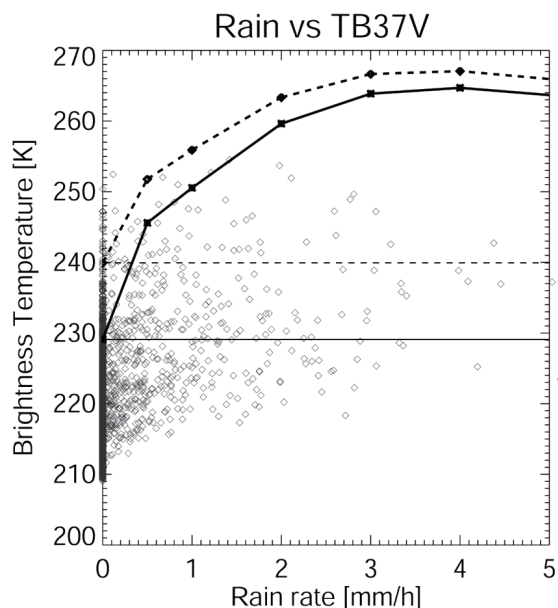


Fig. 13. Scatter plot of the PR surface precipitation rate and TB37V for the case depicted in Fig. 12. The dashed line is the relation between the rainfall rate and TB37V in the original LUT. The solid line is the relation between the rainfall rate and TB37V in the modified LUT.

also given in the figure. TB37Vo, which is TB37V at 0 mm h⁻¹ in the LUTs (the dashed horizontal line in Fig. 13), is higher than the observed TB37V for most of the PR rain pixels, leading to a failure to detect the shallow rain using condition (10).

The PR rain-type classification algorithm (2A23; Awaka et al. 2007; Awaka et al. 2009) detects shallow rain with storm heights much lower than the freezing level. Shallow rain consists of shallow isolated rain and shallow non-isolated rain. When a region of shallow rain is isolated from other non-shallow rain areas, this shallow rain is referred to as shallow isolated rain. Shallow non-isolated rain is defined as shallow rain that is not shallow isolated. The pixel counts for shallow non-isolated rain and shallow-isolated rain are given in Figs. 14a and 14b. Over the mid-latitudes, most of the shallow rain is shallow non-isolated, indicating that it is accompanied by extratropical frontal systems as in case 1 (Fig. 6). Over the sub-tropical ocean, the shallow rain is shallow isolated because the mean descending branch of the meridional Hadley cell suppresses the convection of clouds. Shallow isolated rain over the sub-tropical oceans and shallow non-isolated rain at mid-latitudes should have different microphysical properties of cloud and precipitation. In the forward calculation, hydrometer profiles classified into ten precipitation types are used (Takayabu and Katayama 2004; Takayabu 2006; Takayabu 2008). Precipitation over the mid-latitudes and sub-tropical

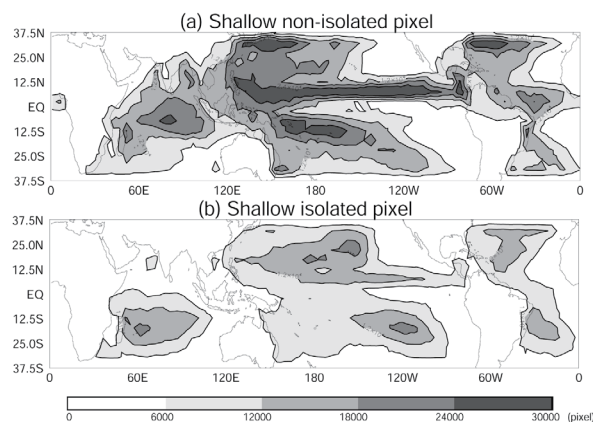


Fig. 14. (a) Shallow non-isolated rain pixel count and (b) shallow isolated rain pixel count in 1999 from the PR 3A25, a 5° spatial-resolution gridded monthly composite of PR 2A25 data.

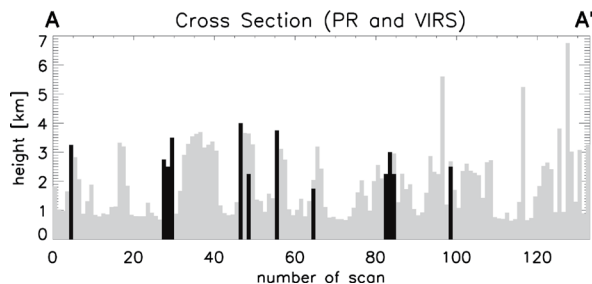


Fig. 15. The same as in Fig. 7 but along line A–A' in Fig. 12a.

oceans is respectively classified as extratropical frontal systems and shallow rain. However, for all precipitation types, it is arbitrarily assumed that there exists a cloud layer with an LWP of 0.5 kg m^{-2} below the freezing-level height, because the distinction between precipitation and cloud and its relationship to the LWP is not entirely understood (see review by Stephens and Kummerow 2007). This assumption may be unrealistic for shallow isolated rain, leading to overestimation of TB37Vo.

The LWP depends on the cloud liquid water content (kg m^{-3}) and the cloud depth. Figure 15 depicts a vertical cross-section along the A–A' line in Fig. 12a. The cloud height is well below the freezing height (4.2 km) and close to the rain-top height. Therefore, we simply parameterize the LWP as a function of the storm height derived from the PR observation. The LWP (kg m^{-2}) is

$$LWP = 0.1 \times SH, \quad (14)$$

where SH (km) is the storm height derived from PR standard product 3A25, a monthly composite of PR 2A25 data with gridded 5-degree spatial resolution. We also parameterize the relative humidity, which was assumed to be 100% below the freezing level. The relative humidity is 100% below the SH and takes on the values from GANAL above the SH. We employ parameterization of the LWP only for the shallow-rain precipitation type. The modified assumptions of the LWP and relative humidity are applied to GSMaP2 in a version we refer to as GSMaP3.

5.2 Performance of GSMaP3

Figure 16 is the result for GSMaP3 over sub-tropical oceans for the same case as in Fig. 11. The ETS value

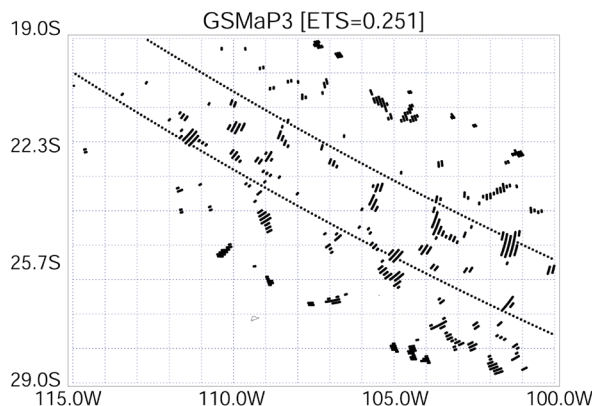


Fig. 16. GSMaP3 for the case depicted in Fig. 12.

of GPROF (GSMaP2) is 0.253 (0.142) (Figs. 12c and 12d). The ETS of GSMaP3 is 0.251 (Fig. 16). The shallow-rain area is detected by GSMaP3 because TB37Vo in the LUT based on the parameterized LWP is lower than the observed TB37V for most of the PR rain pixels (solid line in Fig. 13).

A global comparison of GSMaP3 and GSMaP1 is performed using the ETS for 1999. Figure 17 illustrates the difference in ETS values between GSMaP3 and GSMaP1, normalized by the ETS of GSMaP1. Over sub-tropical oceans, GSMaP3 performs better than GSMaP1 because the assumptions of LWP and relative humidity are better parameterized over sub-tropical oceans, where shallow isolated rain is predominant. A Hovmöller diagram of the zonal average of the ETS values in 1999 shows that the ETS of GSMaP3 is higher than that of GSMaP1 through the whole year. Figure 18 presents a global comparison between GPROF and GSMaP3 in 1999. Figure 18 demonstrates that the ETS of GSMaP3 improves over sub-tropical oceans where the ETS of GSMaP2 is very much lower than that of GPROF. This is because regions of shallow isolated rain, where detection failed in GSMaP2, can be detected by GSMaP3. A Hovmöller diagram of the zonal average ETS values of GSMaP3 and GPROF indicates that GSMaP3 performs as well as GPROF over the sub-tropical ocean.

6. Conclusion

We revised the RNC method of GSMaP (GSMaP1). First, we use 37-GHz emission signatures more efficiently over the ocean to detect shallow rain in retrievals by the GSMaP algorithm. This revised RNC

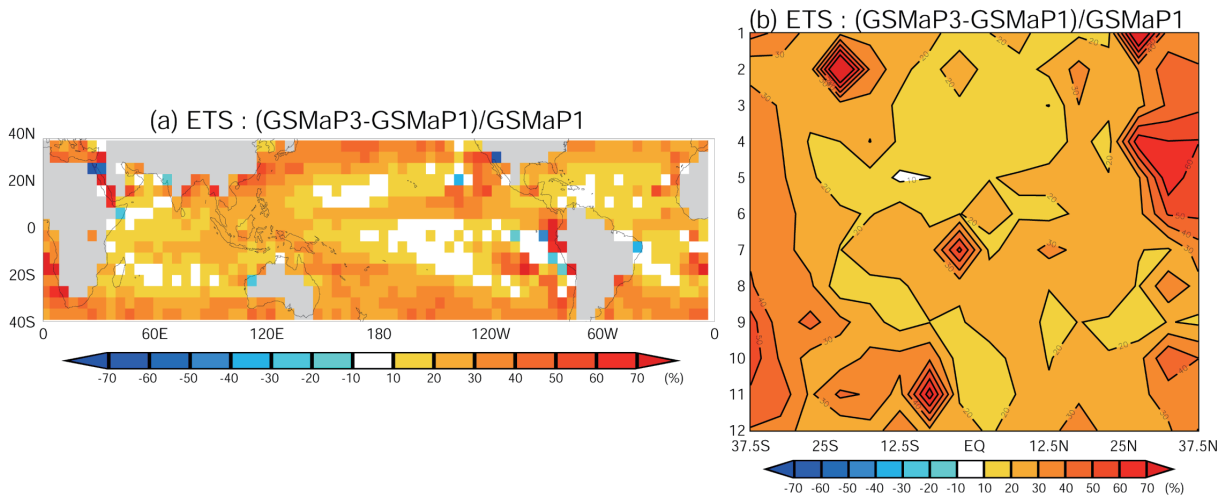


Fig. 17. (a) Global map of the ETS difference between GSMaP3 and GSMaP1, normalized by the ETS of GSMaP1 in 1999. (b) Hovmöller diagram of the monthly zonal average of the ETS difference between GSMaP3 and GSMaP1, normalized by the ETS of GSMaP1 in 1999.

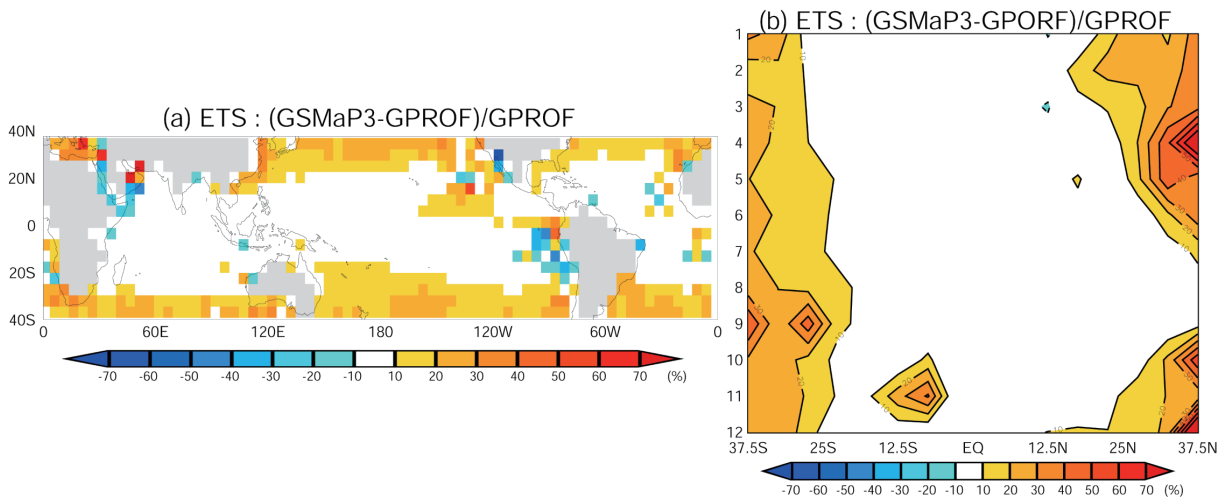


Fig. 18. (a) ETS difference between GSMaP3 and GPROF, normalized by the ETS of GPROF in 1999. (b) Hovmöller diagram of the monthly zonal average of the ETS difference between GSMaP3 and GPROF, normalized by the ETS of GPROF in 1999.

method is called GSMaP2. Second, we parameterize an LWP as a function of storm height (SH) derived from PR observations to detect shallow isolated rain in the forward model. The parameterization of the LWP is introduced into GSMaP2. This further revised RNC method is called GSMaP3. The performance of GSMaP2 and GSMaP3 is investigated using case

studies and global comparisons.

In the case of scattered shallow rain behind cold fronts, GSMaP2 performs better than both GSMaP1 and GPROF because the scattered shallow rain, which is undetectable in GSMaP1 and GPROF, can be detected in GSMaP2. The threshold value of TB37V over rain-free regions, which distinguishes precip-

itation from cloud, is better computed using GANAL in GSMaP2. Therefore, shallow rain is detected using the 37V emission signature in GSMaP2. In the case of typhoon Olga, an improvement from GSMaP1 to GSMaP2 was the elimination of the spurious identification of deep rain. Windy areas are misidentified as rainy regions in GSMaP1 owing to the high sensitivity of TB37H to wind speed. In GSMaP2, a windy region with non-precipitation is correctly identified because TB37V is used instead of P37 for the RNC. The ETS of GSMaP2 is higher than that of GPROF because GPROF produces a larger rainy region than the PR. Most of the regions classified as “possibly rain” by GPROF are raining regions, because the database that is used in the full Bayesian algorithm represents only a small fraction of the systems that might be observed by the TMI.

A global comparison between GSMaP1 and GSMaP2 reveals that GSMaP2 performs better than GSMaP1 over the mid-latitudes and tropics because GSMaP2 has improved the RNC for scattered shallow rain and windy areas. Through the whole year, GSMaP2 improves over the mid-latitudes, but is worse than GSMaP1 over sub-tropical oceans because the detection of shallow isolated rain fails over the sub-tropical oceans. The highest ETS of GSMaP2 occurs during winter in the mid-latitudes. In contrast, the lowest ETS of GSMaP2 occurs during winter over sub-tropical oceans. A global comparison between GSMaP2 and GPROF indicates that GSMaP2 produces a higher ETS than GPROF over mid-latitudes. A threshold value for the RNC using GANAL is computed for each region in GSMaP2, while GPROF globally sets a constant threshold value. Over the mid-latitudes, there is a horizontal non-uniformity of environments because the mid-latitudes are affected by strong baroclinic waves and fronts during the winter. Therefore, GSMaP2 performs better than GPROF. In the future, there will be more opportunities to make observations of higher latitudes from satellites (e.g., the Global Precipitation Measurement project) (Smith et al. 2007), so achieving higher accuracy in the detection of rain at higher latitudes is important.

Although GSMaP2 performs well over the mid-latitudes, its performance becomes worse than that of GSMaP1 over sub-tropical oceans. Over the mid-latitudes, most shallow rain is non-isolated because the shallow rain is accompanied by extratropical frontal systems. In contrast, over sub-tropical oceans, shallow rain is shallow isolated because the mean descending branch of the meridional Hadley cell suppresses the

convection of clouds. In GSMaP, it is arbitrarily assumed that there exists a cloud layer with an LWP of 0.5 kg m^{-2} below the freezing level. This assumption may be unrealistic for shallow isolated rain, and may lead to overestimation of TB37Vo in the forward calculation. Therefore, we parameterize the LWP as a function of SH derived from the PR standard product 3A25 over the region. The detection of the shallow rain in GSMaP3 agrees with the RNC of the PR observation over the sub-tropical ocean because the shallow isolated rain, which is not detected with GSMaP2, can be detected using TB37V.

A global comparison of GSMaP3 and GSMaP1 shows that the ETS of GSMaP3 improves over the sub-tropical oceans because the LWP is better parameterized there and the shallow isolated rain can be detected. Through the whole year, the ETS of GSMaP3 is higher than that of GSMaP1 over almost every region. A global comparison between GSMaP3 and GPROF shows that the ETS of GSMaP3 improves over sub-tropical oceans, where the ETS of GSMaP2 is very much lower than that of GPROF, because regions of shallow isolated rain that GSMaP2 failed to detect can be detected by GSMaP3. Through the whole year, GSMaP3 performs as well as GPROF over sub-tropical oceans, although there are a few regions with lower ETS values for GSMaP3 than for GPROF in winter owing to simple parameterization of the LWP.

In this study, we parameterize the LWP as a function of SH from PR 3A25 only for shallow rain. We consider that the parameterization of the LWP in the forward model is imperfect because observations of the LWP are still inadequate. Therefore, further investigation of the distinction between precipitation and cloud and its relationship to the LWP is needed. For the investigation, it is planned to use the cloud profiling radar (CPR) on Cloudsat (Stephens et al. 2002).

Acknowledgements

This study was supported by the Japan Science and Technology Corporation Core Research for Evolutional Science and Technology. This study was also supported by the Japan Aerospace Exploration Agency Earth Observation Research Center (JAXA EORC) TRMM project and by the Mitsui & Co., Ltd. Environment Fund. The authors would like to thank Professor T. Manabe (Osaka Prefecture University) and Dr. T. Iguchi (NICT) for valuable comments. The authors also thank Dr. C. Kummerow for providing

the TMI2A12 V6 (GPROF) algorithm code and Dr. B. Olson for valuable comments. We would also like to thank the two anonymous reviewers for their valuable comments.

References

- Adler, R., G. Huffman, and P. Keehn, 1994: Global tropical rain estimates from microwave-adjusted geosynchronous IR data. *Remote Sens. Rev.*, **11**, 125–152.
- Aonashi, K., A. Shibata, and G. Liu, 1996: An over-ocean precipitation retrieval using SSM/I multichannel brightness temperatures. *J. Meteor. Soc. Japan*, **74**, 617–637.
- Aonashi, K., and G. Liu, 2000: Passive microwave precipitation retrievals using TMI during the Baiu period of 1998. Part I: Algorithm description and validation. *J. Appl. Meteor.*, **45**, 2259–2275.
- Aonashi, K., J. Awaka, M. Hirose, T. Kozu, T. Kubota, G. Liu, S. Shige, S. Kida, S. Seto, N. Takahashi, and Y. N. Takayabu, 2009: GSMaP passive microwave precipitation retrieval algorithm: Algorithm description and validation. *J. Meteor. Soc. Japan*, **87A**, 119–136.
- Awaka, J., T. Iguchi, and K. Okamoto, 2007: Rain type classification algorithm. *Measuring precipitation from space—EURAINSAT and the future*, V. Levizzani, P. Bauer, and F. J. Turk, Eds., Springer, 213–224.
- Awaka, J., T. Iguchi, and K. Okamoto, 2009: TRMM PR standard algorithm 2A23 and its performance on bright band detection. *J. Meteor. Soc. Japan*, **87A**, 31–52.
- Berg, W., T. L'Ecuyer, and C. Kummerow, 2006: Rainfall climate regimes: The relationship of regional TRMM rainfall biases to the environment. *J. Appl. Meteor. Climatol.*, **45**, 434–454.
- Iguchi, T., 2007: Space-borne radar algorithms, *Measuring precipitation from space—EURAINSAT and the future*, V. Levizzani, P. Bauer, and F. J. Turk, Eds., Springer, 199–212.
- Iguchi, T., T. Kozu, J. Kwiatkowski, R. Meneghini, J. Awaka, and K. Okamoto, 2009: Uncertainties in the rain profiling algorithm for the TRMM Precipitation Radar. *J. Meteor. Soc. Japan*, **87A**, 1–30.
- Karstens, U., C. Simmer, and E. Ruprecht, 1994: Remote sensing of cloud liquid water. *Meteor. Atmos. Phys.*, **54**, 157–171.
- Kozu, T., T. Kawanishi, H. Kuroiwa, M. Kojima, K. Oikawa, H. Kumagai, K. Okamoto, M. Okumura, H. Nakatsuka, and K. Oikawa, 2001: Development of Precipitation Radar onboard the Tropical Rainfall Measuring Mission satellite. *IEEE Trans. Geosci. Remote Sens.*, **39**, 102–116.
- Kubota, T., S. Shige, H. Hashizume, K. Aonashi, N. Takahashi, S. Seto, M. Hirose, Y. Takayabu, T. Ushio, K. Nakagawa, K. Iwanami, M. Kachi, and K. Okamoto, 2007: Global precipitation map using satellite-borne microwave radiometers by the GSMaP Project: Production and Validation. *IEEE Trans. Geosci. Remote Sens.*, **45**, 2259–2275.
- Kummerow, C., W. Barnes, T. Kozu, J. Shiue, and J. Simpson, 1998: The Tropical Rainfall Measuring Mission (TRMM) sensor package. *J. Atmos. Oceanic Technol.*, **15**, 809–817.
- Liu, G., 1998: A fast and accurate model for microwave radiance calculation. *J. Meteor. Soc. Japan*, **76**, 335–343.
- Okamoto, K., 2003: A short history of the TRMM Precipitation Radar. *Cloud Systems, Hurricanes and the Tropical Rainfall Measurement Mission (TRMM): A Tribute to Dr. Joanne Simpson.*, No. **51**, Amer. Meteor. Soc., 187–195.
- Okamoto, K., and S. Shige, 2008: TRMM Precipitation Radar and its observation results. *IEICE Trans. Commun. Japan*, **J91-B**, 723–733, (in Japanese).
- Olson, W. S., C. D. Kummerow, S. Yang, G. W. Petty, W.-K. Tao, T. L. Bell, S. A. Braun, Y. Wang, S. E. Lang, D. E. Johnson, and C. Chiu, 2006: Precipitation and latent heating distributions from satellite passive microwave radiometry. Part I: Improved method and uncertainties. *J. Appl. Meteor. Climatol.*, **45**, 702–720.
- Petty, G., 1994: Physical retrievals of over-ocean rain rate from multichannel microwave imagery. Part I: Theoretical characteristics of normalized polarization and scattering indices. *Meteor. Atmos. Phys.*, **54**, 79–99.
- Petty, G., 1997: An intercomparison of oceanic precipitation frequencies from 10 SSM/I rain rate algorithms and shipboard present-weather reports. *J. Geophys. Res.*, **102**, 1757–1777.
- Schaefer, J. T., 1990: The critical success index as an indicator of warning skill. *Wea. Forecasting*, **5**, 570–575.
- Seto, S., N. Takahashi, and T. Iguchi, 2005: Rain/no-rain classification methods for microwave radiometer observations over land using statis-

- tical information for brightness temperatures under no-rain conditions. *J. Appl. Meteor.*, **44**, 1243–1259.
- Shige, S., T. Watanabe, H. Sasaki, T. Kubota, S. Kida, and K. Okamoto, 2008: Validation of western and eastern Pacific rainfall estimates from the TRMM PR using a radiative transfer model. *J. Geophys. Res.*, **113**, D15116, doi:10.1029/2007JD009002.
- Smith, E. A., G. Asrar, Y. Furuhashi, A. Ginati, C. Kummerow, V. Levizzani, A. Mugnai, K. Nakamura, R. Adler, V. Casse, M. Cleave, M. Debois, J. Durning, J. Entin, P. Houser, T. Iguchi, R. Kakar, J. Kaye, M. Kojima, D. Lettenmaier, M. Luther, A. Mehta, P. Morel, T. Nakazawa, S. Neeck, K. Okamoto, R. Oki, G. Raju, M. Shepherd, E. Stocker, J. Testud, and E. Wood, 2007: International Global precipitation measurement (GPM) program and mission: an overview, *Measuring precipitation from space - EURAINSAT and the future*, V. Levizzani, P. Bauer, and F. J. Turk, Eds., Springer, 611–633.
- Spencer, R., H. Goodman, and R. Hood, 1989: Precipitation retrieval over land and ocean with the SSM/I: Identification and characteristics of the scattering signal. *J. Atmos. Oceanic Technol.*, **6**, 254–273.
- Stephens, G. L., D. G. Vane, R. J. Boain, G. G. Mace, K. Sassen, Z. Wang, A. J. Illingworth, E. J. O'Connor, W. B. Rossow, S. L. Durden, S. D. Miller, R. T. Austin, A. Benedetti, and C. Mitrescu, 2002: The cloudsat mission and the a-train. *Bull. Amer. Meteor. Soc.*, **83**, 1771–1790.
- Stephens, G. L., and C. D. Kummerow, 2007: The remote sensing of clouds and precipitation from space: A review, *J. Atmos. Sci.*, **64**, 3742–3765.
- Takayabu, T., 2006: Rain-yield per flash calculated from TRMM PR and LIS data and its relationship to the contribution of tall convective rain. *Geophys. Res. Lett.*, **33**, L18705, doi:10.1029/2006GL027531.
- Takayabu, T., and M. Katayama, 2004: Low-latitudes rainfall characteristics and its meteorological factors analyzed with mesoscale statistics of TRMM PR data, presented at the 1st AOGS, Singapore, Paper 57-OOA–A1683.
- Takayabu, Y. N., 2008: Observing rainfall regimes using TRMM PR and LIS data. *GEWEX News*, **18**, No. 2, 9–10.
- Wilheit, T. T., A. T. C. Chang, and L. S. Chiu, 1991: Retrieval of monthly rainfall indices from microwave radiometric measurements using probability distribution functions. *J. Atmos. Oceanic Technol.*, **8**, 118–136.
- Wilks, D. S., 1995: *Statistical Methods in the Atmospheric Sciences*. Academic Press, 263 pp.

